The International Journal of Advanced Manufacturing Technology (2021) 115:2325–2342
https://doi.org/10.1007/s00170-021-07302-0

ORIGINAL ARTICLE

Research on the milling stability of thin-walled parts based on the semi-discretization method of improved Runge-Kutta method

Muxuan Guo[1] · Lida Zhu[1] · Boling Yan[1] · Zhihong Guan[1]

Received: 14 October 2020 / Accepted: 17 May 2021 / Published online: 24 May 2021

Abstract
Chatter is a very common phenomenon in the milling process. The occurrence of chatter will cause chatter marks on the processed surface, cause the tool to jump, and even bring sharp and harsh noise, making the processed surface unable to meet the accuracy requirements. Thin-walled parts are more prone to chatter due to their lower stiffness. In order to avoid the occurrence of chatter, this paper adopts the method of combining theoretical analysis with milling experiments to conduct in-depth research on the prediction of chatter. Considering the first-order and second-order modal parameters of the tool and thin-walled part as well as the specific processing parameters, based on the milling dynamics model, a semi-discretization method based on the improved Runge-Kutta method (IRKM-SDM) is used to draw the chatter stability lobe diagram. Through simulation and experiments, it is proved that in terms of simulation accuracy and calculation speed, compared with the zero-order analysis (ZOA), multi-frequency solution (MFS), and the traditional semi-discretization method (SDM), the stability lobe diagram obtained by the IRKM-SDM is more advantageous. This study is of great significance for optimizing cutting parameters and suppressing chatter in the actual machining process.

Keywords Chatter · Thin-walled parts · Semi-discretization method · Improved Runge-Kutta · Stability lobe diagram

1 Introduction

In mechanical vibration, the vibration in the metal cutting process is defined as five situations, free vibration, forced vibration, random vibration, mixed vibration, and self-excited vibration [1, 2]. Regenerative chatter is a type of self-excited vibration. In the normal processing process, after the last cutter tooth is processed, it will leave chatter marks on the processing surface. The processing position of the latter cutter tooth is consistent with the previous cutter tooth, and the chatter marks are also left. Since the current cutter tooth processes the inner surface and the previous cutter tooth processes the outer surface, the workpiece feed and the rotation of the tool will cause a phase difference in the chatter marks of the inner and outer surfaces, thereby causing a change in cutting thickness. During the milling process, such a phase difference will be continuously generated to provide continuous and undecayed energy input for regenerative chatter. Therefore, it can be said that regenerative chatter is the most direct factor that causes processing instability. Moreover, among the many causes of chatter, regenerative chatter is the most harmful.

In view of the chatter phenomenon generated during the machining process, currently stability lobe diagrams are commonly used for prediction to avoid cutting chatter. In 1995, Altintas and Budak [3] proposed the zero-order analysis (ZOA) for chatter stability. This method adopted Fourier series to approximate the time varying dynamic cutting force coefficients and directly calculated the axial depth of the chatter free axial depth of cuts and the spindle speed from the proposed linear analytical expression set. Bayly et al. [4] used the ZOA, time finite element analysis method, and time-marching simulation method to determine the stable boundary of the 2 DOF milling process and made a comparison. The results showed that the ZOA has the fastest simulation speed, but the accuracy is problematic under the condition of small radial depth of cut. Compared with the time-marching simulation method, the time finite element analysis method is more

✉ Lida Zhu
neulidazhu@163.com

[1] School of Mechanical Engineering and Automation, Northeastern University, Shenyang 110819, China

efficient and can achieve accurate prediction under the condition of small radial depth of cut. In order to solve the problem that the ZOA cannot accurately predict the stable boundary of chatter under the condition of small radial depth of cut, Merdol and Altintas [5] proposed a multi-frequency solution (MFS) of chatter stability, considering harmonics of the tooth passing frequencies. Insperger and Stépán [6, 7] proposed a semi-discretization method (SDM) for analyzing the stability of linear delayed systems, and made improvements to this, and established a stability diagram of a 2 DOF milling model. Ding et al. [8, 9] proposed a full-discretization method (FDM) for milling stability prediction based on direct integration method, discussed the efficiency of the method, and verified the effectiveness of the algorithm.

Li et al. [10] introduced an extended dynamic model of milling system considering regeneration, helix angle, and process damping into the high-order time domain algorithm for the processing chatter of titanium alloy thin-walled parts to ensure the stability of the lobe diagram simulation efficiency and precision. Liu et al. [11] combined the process damping model with the ZOA method to establish a stability lobe diagram and verified the correctness of the model through simulation and experiment. The results showed that at low speeds, considering the effect of process damping, the stable area will increase significantly. Wu et al. [12] used aluminum alloy 7075-T6 thin-walled parts which fixed at both ends as the research object, and took the maximum Lyapunov exponent 0.61 of the vibration signal as the nonlinear criterion of milling chatter. The milling contour lines method was used to obtain the chatter stability critical curve. Ma et al. [13] studied the influence of cutter runout on the milling stability lobe diagram when multiple modes occur. Simulation and experimental results showed that the occurrence of cutter runout can locally increase the stable region. Based on the finite difference method and extrapolation method, Zhang et al. [14] proposed a numerical differentiation method to predict the high speed milling stability of a two degrees of freedom (DOF) system and demonstrated the effectiveness and efficiency of the proposed method through experiment. Ozoegwu et al. [15] established a multiplicity model of radial immersion and proved that the split of effective radial immersion can cause the stability boundary curve to shift significantly to a higher axial depth. Comak et al. [16] used the SDM employing multiple delays to model and solve dynamics and stability of variable pitch and helix tools and selected the optimum pitch and helix angles. According to the stability lobe diagram, the stability depth of the cut limits could be significantly improved, and the simulation results were verified through chatter experiments. Hajdu et al. [17] based on the concepts of stability radius and structured singular values, combined with extended MFS, proposed a frequency domain method to achieve robust stability lobe diagram simulation to ensure the stability against bounded uncertainties and perturbations. Based on the Newton interpolation polynomial and an improved precise time integration (PTI) algorithm, Jiang et al. [18] proposed a second-order SDM for efficiently and accurately predicting the stability of the milling process and verified the method from both computational efficiency and accuracy. Jafarzadeh et al. [19] incorporated various nonlinear phenomena in the cutting process related to cutting forces, friction, and tool geometry and proposed a finite element model of orthogonal chip formation combined with machine tool dynamics to study and compare the two major mechanisms of chatter, namely, the regeneration of waviness and mode coupling. Dai et al. [20, 21] used explicit precise integration method (PIM) to predict the chatter stability of the milling process, constructed a stability lobe diagram, and verified the effectiveness of the method. Zhu and Liu et al. [22, 23] studied regenerative chatter and mode coupling chatter and proposed a milling chatter detection method based on variational mode decomposition (VMD) and energy entropy and based on kurtosis to select number of modes (K) and the quadratic penalty (α) in VMD decomposition. Simulation and experimental results showed that this method can effectively detect chatter. Sun et al. [24] proposed an accurate modeling method for dynamic milling systems with force-induced deformation effects. The extended second-order SDM was used to predict the chatter stability of the system, and the effectiveness of the method was verified by milling experiments. Zhou et al. [25] optimized the fourth-order FDM in consideration of the helix angle and multi-mode. From the calculation results, it could be seen that the stability lobe diagrams obtained by this method are superior to the stability lobe diagrams obtained by the existing FDMs in convergence speed and calculation efficiency. Kiss et al. [26] proposed an improved prediction method, using the modulus of the dominant Floquet multiplier to estimate the stability lobe diagram and conducted experimental verification. Wan et al. [27] established a dynamic model with varying time delay caused by the vibration assistance and used a SDM to determine the chatter stability at different frequencies and amplitudes of vibration assistance. The simulation results showed that the vibration assistance does not improve the critical depth of cut but generates new stability lobes between the original two adjacent lobes corresponding to no vibration assistance. Yang et al. [28] aimed at the prediction problem of chattering for finishing and semi-finishing of large thin-walled structures, proposed an effective decomposition-condensation method to predict the in-process workpiece (IPW) dynamics, and integrated this method into a dynamic model. Experimental results showed that, under the same calculation accuracy, the proposed method reduces the amount of calculation by twice compared with the existing chatter prediction methods. Dun et al. [29] proposed a numerical difference method based on Adams-Bashforth scheme and multi-modal scheme of numerical methods and verified the critical stability boundaries predicted by analytical and

numerical methods through milling experiments. Chen et al. [30] established a micro-grinding force model considering the nonlinear change of the cutting coefficients caused by the feed rate and the process damping effect in the shearing-dominant regimes and verified the accuracy of the proposed model through experiments.

In this paper, a semi-discretization method based on the improved Runge-Kutta method (IRKM-SDM) is proposed, and the stability limit simulation is carried out for aluminum alloy thin-walled parts, considering the modal parameters of the tool and the workpiece. Through milling experiments, the simulation accuracy of the method in this paper is verified. The simulation and experimental results show that compared with other methods, the method in this paper has better simulation accuracy and calculation speed.

2 Chatter stability semi-discretization method based on second-order Runge-Kutta method

2.1 2 DOF milling equation

In order to improve the simulation accuracy and calculation speed of the lobe diagram, this paper improves the semi-discretization algorithm of chatter stability based on Runge-Kutta method. The dynamic model of the 2 DOF milling system can be expressed as:

$$\begin{pmatrix}\ddot{x}(t)\\ \ddot{y}(t)\end{pmatrix}+\begin{pmatrix}2\zeta\omega_n & 0\\ 0 & 2\zeta\omega_n\end{pmatrix}\begin{pmatrix}\dot{x}(t)\\ \dot{y}(t)\end{pmatrix}+\begin{pmatrix}\omega_n^2+\dfrac{a_p h_{xx}(t)}{m_t} & \dfrac{a_p h_{xy}(t)}{m_t}\\ \dfrac{a_p h_{yx}(t)}{m_t} & \omega_n^2+\dfrac{a_p h_{yy}(t)}{m_t}\end{pmatrix}\begin{pmatrix}x(t)\\ y(t)\end{pmatrix}=\begin{pmatrix}\dfrac{a_p h_{xx}(t)}{m_t} & \dfrac{a_p h_{xy}(t)}{m_t}\\ \dfrac{a_p h_{yx}(t)}{m_t} & \dfrac{a_p h_{yy}(t)}{m_t}\end{pmatrix}\begin{pmatrix}x(t-T)\\ y(t-T)\end{pmatrix} \tag{1}$$

In Eq. (1), ω_n is the natural frequency of the system, ζ is the damping ratio of the system, m_t is the modal mass, and a_p is the axial depth of cut. Generally speaking, for tools, assuming that the tools are symmetrical, the modal mass of the tools in the x and y directions are considered equal.

In Eq. (1), $h_{xx}(t)$, $h_{xy}(t)$, $h_{yx}(t)$, and $h_{yy}(t)$ are the four projections of the specific cutting force coefficient, which can be expressed as:

$$\begin{cases} h_{xx}(t)=\sum_{j=1}^{N} g(\phi_j(t))\sin(\phi_j(t))\left(K_t\cos(\phi_j(t))+K_n\sin(\phi_j(t))\right)\\ h_{xy}(t)=\sum_{j=1}^{N} g(\phi_j(t))\cos(\phi_j(t))\left(K_t\cos(\phi_j(t))+K_n\sin(\phi_j(t))\right)\\ h_{yx}(t)=\sum_{j=1}^{N} g(\phi_j(t))\sin(\phi_j(t))\left(-K_t\sin(\phi_j(t))+K_n\cos(\phi_j(t))\right)\\ h_{yy}(t)=\sum_{j=1}^{N} g(\phi_j(t))\cos(\phi_j(t))\left(-K_t\sin(\phi_j(t))+K_n\cos(\phi_j(t))\right)\end{cases} \tag{2}$$

In Eq. (2), K_t is the tangential cutting force coefficient, and K_n is the radial force cutting coefficient. $\phi_j(t)$ is the contact angle of the jth tooth, which can be expressed as:

$$\phi_j(t)=\frac{\pi}{60}nt+(j-1)\phi_p \tag{3}$$

In Eq. (3), $n(rpm)$ is the spindle speed, and $\phi_p=\frac{2\pi}{N}$ is the angle between the cutter teeth. N is the number of cutter teeth. $g(\phi_j)$ is a unit step function, used to judge whether the tool is in the machining state, which can be expressed as:

$$g(\phi_j)=\begin{cases}0, \phi_j<\phi_{st}\text{或}\phi_j>\phi_{ex}\\ 1, \phi_{st}\le\phi_j\le\phi_{ex}\end{cases} \tag{4}$$

When $g(\phi_j)=1$, the tool is cutting; when $g(\phi_j)=0$, the tool is not cutting. Among them, ϕ_{st} and ϕ_{ex} are the contact angles when the tool is cut in and out, respectively. When adopting the method of down-milling, ϕ_{st} and ϕ_{ex} can be expressed as:

$$\begin{cases}\phi_{st}=\arccos\left(\dfrac{2a_e}{D}-1\right)\\ \phi_{ex}=\pi\end{cases} \tag{5}$$

When adopting the method of up-milling, it can be expressed as:

$$\begin{cases}\phi_{st}=0\\ \phi_{ex}=\arccos\left(1-\dfrac{2a_e}{D}\right)\end{cases} \tag{6}$$

In Eq. (5) and Eq. (6), a_e is the radial depth of cut and D is the tool diameter.

Equation (1) can be rewritten as:

$$\dot{X}(t)=A(t)X(t)+B(t)X(t-T) \tag{7}$$

where

$$X(t)=\begin{pmatrix} x(t) \\ y(t)\ (t)\dot{y}(t) \\ \dot{x} \end{pmatrix} \text{ and } \dot{X}(t)=\begin{pmatrix} \dot{x}(t)\dot{y}(t)\ddot{x}(t)\ddot{y}(t) \end{pmatrix} \quad (8)$$

$$A(t)=\begin{pmatrix} 0 & 0 & 1 & 0 \\ 0 & 0 & 0 & 1 \\ -\omega_n^2-\dfrac{a_p h_{xx}(t)}{m_t} & -\dfrac{a_p h_{xy}(t)}{m_t} & -2\zeta\omega_n & 0 \\ -\dfrac{a_p h_{yx}(t)}{m_t} & -\omega_n^2-\dfrac{a_p h_{yy}(t)}{m_t} & 0 & -2\zeta\omega_n \end{pmatrix} \quad (9)$$

$$B(t)=\begin{pmatrix} 0 & 0 & 0 & 0 \\ 0 & 0 & 0 & 0 \\ \dfrac{a_p h_{xx}(t)}{m_t} & \dfrac{a_p h_{xy}(t)}{m_t} & 0 & 0 \\ \dfrac{a_p h_{yx}(t)}{m_t} & \dfrac{a_p h_{yy}(t)}{m_t} & 0 & 0 \end{pmatrix} \quad (10)$$

$A(t)$ and $B(t)$ are periodic matrices, with $A(t)=A(t+T)$, $B(t)=B(t+T)$. T is the time period. For the milling process, the time delay is equal to the time period, with $T=\tau$. For the spindle speed $n(rpm)$, the time delay and time period are $\tau=T=\frac{60}{Nn}(s)$, and the time step is $\Delta t=T/m=60/(mNn)$. m is the discretization number of time.

Based on the idea of the SDM, in the ith semi-discretization interval, Eq. (1) can be approximated as:

$$\begin{pmatrix} \ddot{x}(t) \\ \ddot{y}(t) \end{pmatrix}+\begin{pmatrix} 2\zeta\omega_n & 0 \\ 0 & 2\zeta\omega_n \end{pmatrix}\begin{pmatrix} \dot{x}(t)\dot{y}(t) \end{pmatrix}+\begin{pmatrix} \omega_n^2+\dfrac{a_p h_{xxi}}{m_t} & \dfrac{a_p h_{xyi}}{m_t} \\ \dfrac{a_p h_{yxi}}{m_t} & \omega_n^2+\dfrac{a_p h_{yyi}}{m_t} \end{pmatrix}\begin{pmatrix} x(t) \\ y(t) \end{pmatrix} = \begin{pmatrix} \dfrac{a_p h_{xxi}}{m_t} & \dfrac{a_p h_{xyi}}{m_t} \\ \dfrac{a_p h_{yxi}}{m_t} & \dfrac{a_p h_{yyi}}{m_t} \end{pmatrix}\begin{pmatrix} x_{T,i} \\ y_{T,i} \end{pmatrix}, t\in[t_i,t_{i+1}] \quad (11)$$

In Eq. (11),

$$\begin{cases} h_{xxi}=\dfrac{1}{\Delta t}\int_{t_i}^{t_{i+1}} h_{xx}(t)dt \\ h_{xyi}=\dfrac{1}{\Delta t}\int_{t_i}^{t_{i+1}} h_{xy}(t)dt \\ h_{yxi}=\dfrac{1}{\Delta t}\int_{t_i}^{t_{i+1}} h_{yx}(t)dt \\ h_{yyi}=\dfrac{1}{\Delta t}\int_{t_i}^{t_{i+1}} h_{yy}(t)dt \end{cases} \quad (12)$$

For definite integration, according to the special division method of n equal divisions:

$$\int_a^b f(x)dx=\lim_{k\to\infty}\sum_{i=1}^{k} f\left[a+\frac{i}{k}(b-a)\right]\frac{b-a}{n} \quad (13)$$

Therefore, an appropriate value of k can be selected to obtain:

$$\begin{cases} h_{xxi}\approx\dfrac{1}{\Delta t}\sum\limits_{i=1}^{k} h_{xx}\left[t_i+\dfrac{i}{k}(t_{i+1}-t_i)\right]\dfrac{t_{i+1}-t_i}{k} \\ h_{xyi}\approx\dfrac{1}{\Delta t}\sum\limits_{i=1}^{k} h_{xy}\left[t_i+\dfrac{i}{k}(t_{i+1}-t_i)\right]\dfrac{t_{i+1}-t_i}{k} \\ h_{yxi}\approx\dfrac{1}{\Delta t}\sum\limits_{i=1}^{k} h_{yx}\left[t_i+\dfrac{i}{k}(t_{i+1}-t_i)\right]\dfrac{t_{i+1}-t_i}{k} \\ h_{yyi}\approx\dfrac{1}{\Delta t}\sum\limits_{i=1}^{k} h_{yy}\left[t_i+\dfrac{i}{k}(t_{i+1}-t_i)\right]\dfrac{t_{i+1}-t_i}{k} \end{cases} \quad (14)$$

Therefore, in the ith semi-discretization interval, Eq. (7) can be rewritten as:

$$\dot{X}(t)=A_i X(t)+B_i X(t-T), t\in[t_i,t_{i+1}] \quad (15)$$

In Eq. (15), $i=0, 1, 2, \ldots\ldots, m$, the initial condition is $X(t_i)=X_i$.

2.2 Second-order Runge-Kutta method

Compared with the fourth-order Runge-Kutta method used in the literatures [31, 32], the second-order Runge-Kutta method reduces the complexity of the algorithm. To use the second-order Runge-Kutta method to solve Eq. (15), it is necessary to select the appropriate time discretization number m to discrete the time period T. The expression of the second-order Runge-Kutta method is as follows:

$$\begin{cases} X_{i+1} = X_i + \dfrac{\Delta t}{2}(K_1 + K_2) \\ K_1 = f(t_i, X_i) \\ K_2 = f(t_i + \Delta t, X_i + K_1) \end{cases} \tag{16}$$

In Eq. (16), $\dot{X}(t) = f(t, X)$, $X_i = X(t_i) = X(i\Delta t)$, $X_i = X(t_i) = X(i\Delta t)$, and $i = 0, 1, 2, \ldots\ldots, m$.

Compared with the previous Runge-Kutta method, the improved Runge-Kutta considers both $X(t)$ and $X(t-T)$ in Eq. (15) as a function of time t. After derivation, the formula of K_1 and K_2 is as follows:

$$\begin{cases} K_1 = A_i X_i + B_i X_{i-m} \\ K_2 = A_{i+1} X_{i+1} + B_{i+1} X_{i+1-m} \end{cases} \tag{17}$$

Substitute K_1 and K_2 into Eq. (16) and organize:

$$\left(I - \frac{\Delta t}{2} A_{i+1}\right) X_{i+1} = \left(I + \frac{\Delta t}{2} A_i\right) X_i + \frac{\Delta t}{2} B_i X_{i-m} + \frac{\Delta t}{2} B_{i+1} X_{i+1-m} \tag{18}$$

Let $P_{i+1,1} = I - \frac{\Delta t}{2} A_{i+1}$, $P_{i,1} = I + \frac{\Delta t}{2} A_i$, $P_{i-m,1} = \frac{\Delta t}{2} B_i$, and $P_{i+1-m,1} = \frac{\Delta t}{2} B_{i+1}$, and Eq. (18) can be transformed into:

$$X_{i+1} = P_{i+1,1}^{-1} P_{i,1} X_i + P_{i+1,1}^{-1} P_{i-m,1} X_{i-m} + P_{i+1,1}^{-1} P_{i+1-m,1} X_{i+1-m} \tag{19}$$

Let $P_{i+1} = P_{i+1,1}^{-1} P_{i,1}$, $P_{i-m} = P_{i+1,1}^{-1} P_{i-m,1}$, and $P_{i+1-m} = P_{i+1,1}^{-1} P_{i+1-m,1}$, and Eq. (19) can be transformed into:

$$X_{i+1} = P_i X_i + P_{i-m} X_{i-m} + P_{i+1-m} X_{i+1-m} \tag{20}$$

It should be noted that since the third column and the fourth column of the matrix B_i and B_{i+1} are both 0, the third and fourth columns of the matrix $P_{i-m,1}$ and $P_{i+1-m,1}$ are both 0. Similarly, we can know that the third and fourth columns of the matrix P_{i-m} and P_{i+1-m} are both 0. Therefore, the calculation of X_{i+1} depends only on $x_{i+1}, y_{i+1}, \dot{x}_{i+1}, \dot{y}_{i+1}, x_{i-m}, y_{i-m}, x_{i+1-m}$, and y_{i+1-m} and has nothing to do with $\dot{x}_{i-m}$, $\dot{y}_{i-m}$, $\dot{x}_{i+1-m}$, and $\dot{y}_{i+1-m}$.

Therefore, a $(2m+4)$ dimensional vector z_i can be defined, expressed as:

$$z_i = col\left(x_i, y_i, \dot{x}_i, \dot{y}_i, x_{i-1}, y_{i-1}, \cdots, x_{i+1-m}, y_{i+1-m}, x_{i-m}, y_{i-m}\right) \tag{21}$$

Using this vector instead of the $4(m+1)$, dimensional vector v_i can reduce the dimension of the discretization map. v_i is expressed as:

$$v_i = col\left(x_i, y_i, \dot{x}_i, \dot{y}_i, x_{i-1}, y_{i-1}, \dot{x}_{i-1}, \dot{y}_{i-1}, \cdots, x_{i-m}, y_{i-m}, \dot{x}_{i-m}, \dot{y}_{i-m}\right) \tag{22}$$

Define the discretization map as:

$$z_{i+1} = H_i z_i \tag{23}$$

Among them, $(2m+4) \times (2m+4)$ dimension matrix H_i is expressed as follows:

$$H_i = \begin{pmatrix} P_{i,11} & P_{i,12} & P_{i,13} & P_{i,14} & 0 & \cdots & 0 & P_{i-m+1,13} & P_{i-m+1,14} & P_{i-m,13} & P_{i-m,14} \\ P_{i,21} & P_{i,22} & P_{i,23} & P_{i,24} & 0 & \cdots & 0 & P_{i-m+1,23} & P_{i-m+1,24} & P_{i-m,23} & P_{i-m,24} \\ P_{i,31} & P_{i,32} & P_{i,33} & P_{i,34} & 0 & \cdots & 0 & P_{i-m+1,33} & P_{i-m+1,34} & P_{i-m,33} & P_{i-m,34} \\ P_{i,41} & P_{i,42} & P_{i,43} & P_{i,44} & 0 & \cdots & 0 & P_{i-m+1,43} & P_{i-m+1,44} & P_{i-m,43} & P_{i-m,44} \\ 1 & 0 & 0 & 0 & 0 & \cdots & 0 & 0 & 0 & 0 & 0 \\ 0 & 1 & 0 & 0 & 0 & \cdots & 0 & 0 & 0 & 0 & 0 \\ 0 & 0 & 0 & 0 & 1 & \cdots & 0 & 0 & 0 & 0 & 0 \\ \vdots & \vdots & \vdots & \vdots & \vdots & \ddots & 0 & 0 & 0 & 0 & 0 \\ 0 & 0 & 0 & 0 & 0 & \cdots & 1 & 0 & 0 & 0 & 0 \\ 0 & 0 & 0 & 0 & 0 & \cdots & 0 & 1 & 0 & 0 & 0 \\ 0 & 0 & 0 & 0 & 0 & \cdots & 0 & 0 & 1 & 0 & 0 \end{pmatrix} \tag{24}$$

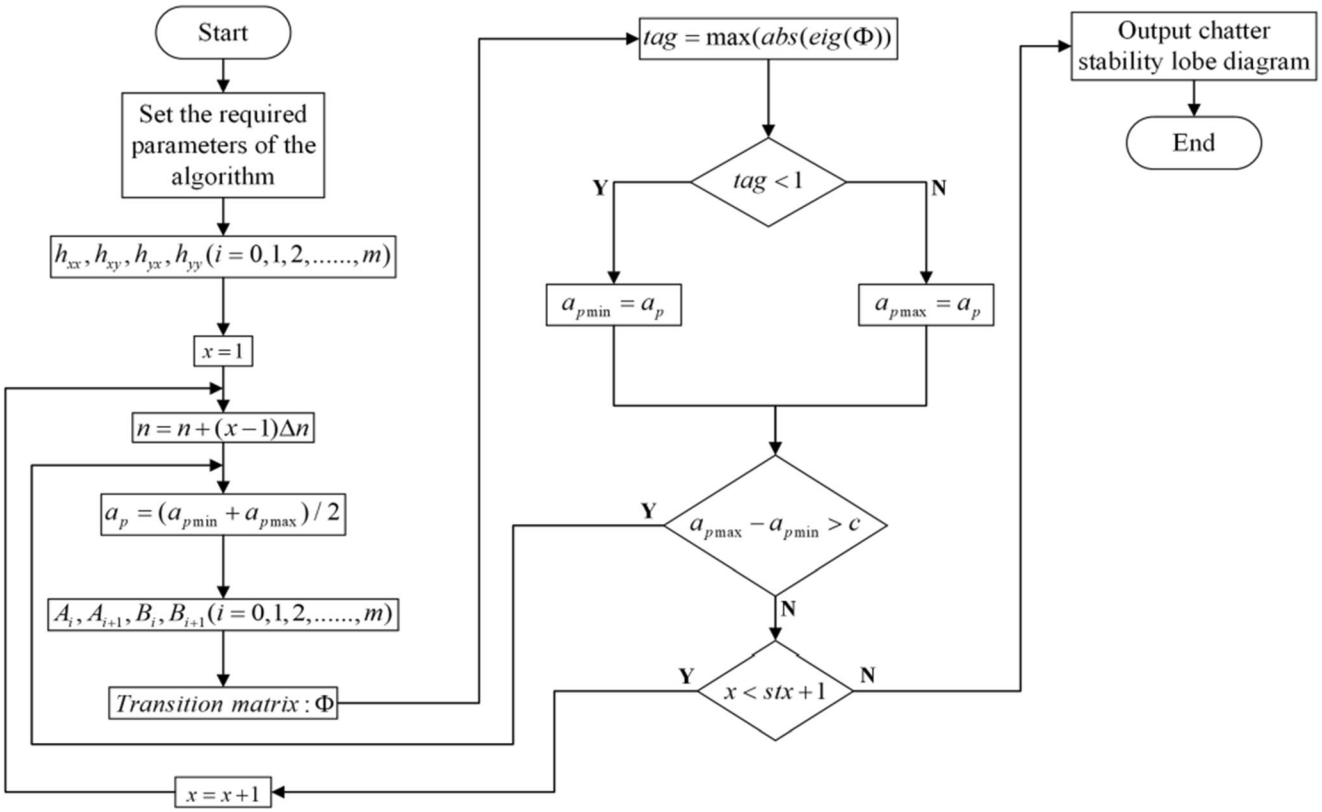

Fig. 1 Simulation flow chart of milling chatter stability lobe diagram based on IRKM-SDM

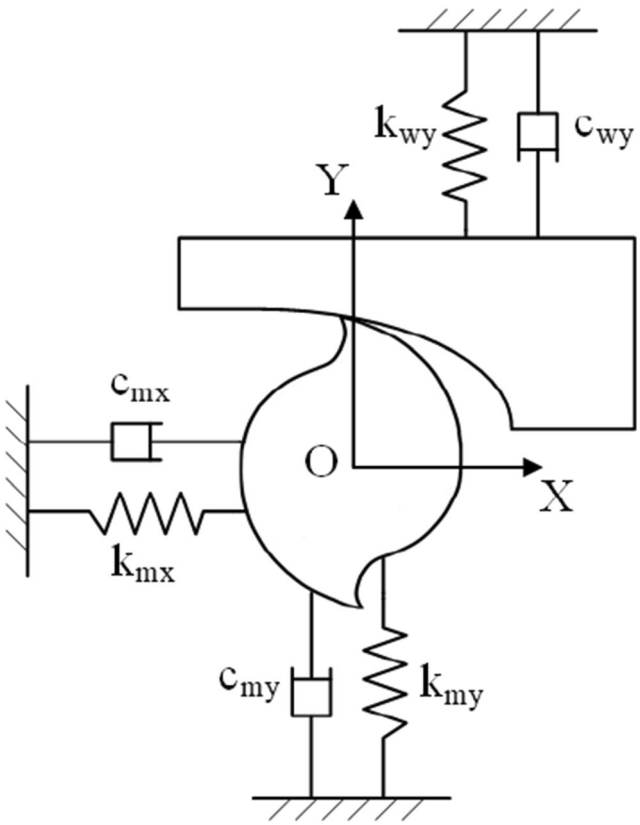

Fig. 2 Tool-workpiece second-order spring damping system

In Eq. (24), $P_{i,\,hl}$, $P_{i-m+1,\,hl}$, and $P_{i-m,\,hl}$ represent the hth row and the lth column of the matrices P_i, P_{i-m+1}, and P_{i-m}, respectively.

Thus, the conversion matrix Φ can be defined as follows:

$$z_m = \Phi z_0 \tag{25}$$

In Eq. (25), $\Phi = H_{m-1}H_{m-2}H_{m-3}\cdots H_1H_0$.

If the eigenvalues of Φ are in modulus less than one, the system is stable at the corresponding speed and axial cutting depth; otherwise, the system will chatter [7].

Introduce the dichotomy method and apply the IRKM-SDM to draw the chatter stability lobe diagram as follows:

(1) Initialize modal parameters, tool parameters, and cutting parameters. At the same time, determine the discretization number m of the period T, the spindle speed range $[n_{\min}, n_{\max}]$, the axial depth of cut range $[0, a_{p\max}]$, the minimum axial depth of cut difference c, and definite integral discrete interval number int _ k.

(2) According to the discrete number m of the period T and the definite integral discrete interval number int _ k, calculate the four projections of the specific cutting force coefficient h_{xxi}, h_{xyi}, h_{yxi}, and $h_{yyi}(i = 0, 1, 2, \ldots\ldots, m)$.

(3) Select the appropriate spindle speed discrete number stx, starting from the minimum spindle speed, take the median axial depth of cut, and gradually calculate the

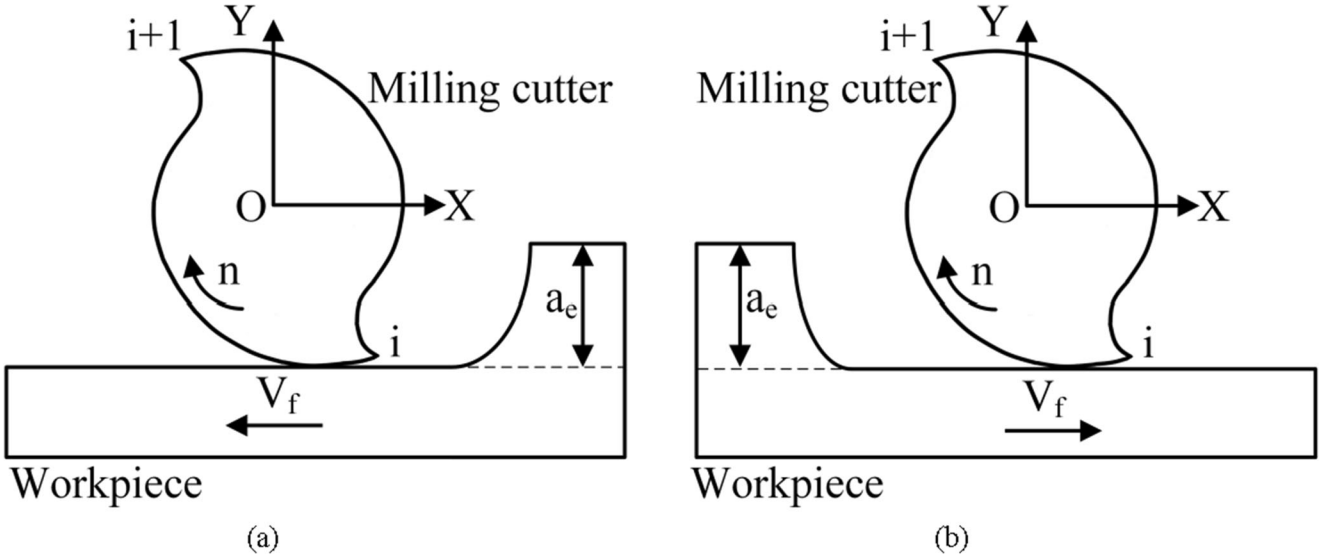

Fig. 3 **a** Down-milling and **b** up-milling conditions of the tool

corresponding matrix A_i, A_{i+1}, B_i, and $B_{i+1}(i = 0, 1, 2, \ldots\ldots, m)$ according to the four projections of the specific cutting force coefficient h_{xxi}, h_{xyi}, h_{yxi}, and $h_{yyi}(i = 0, 1, 2, \ldots\ldots, m)$.

(4) According to the obtained matrix A_i, A_{i+1}, B_i, and $B_{i+1}(i = 0, 1, 2, \ldots\ldots, m)$, generate a transformation matrix Φ.

(5) Find the modulus of the eigenvalues of matrix Φ. If the eigenvalues of Φ are in modulus less than 1, the current axial depth of cut is taken as the minimum value. If the eigenvalues of Φ are in modulus greater than or equal to 1, the current axial depth of cut is taken as the maximum value.

(6) Calculate the difference between the maximum and minimum axial depth of cut. If the difference is less than the minimum axial depth of cut difference c, the median axial depth of cut at this time is the critical axial depth of cut at the current speed. Otherwise, go back to step (3).

(7) Draw the critical axial depth of cut corresponding to different spindle speeds together to obtain the chatter stability lobe diagram.

The simulation flow chart is shown in Fig. 1.

3 Modal experiment and analysis of tool-workpiece system

When the machining parameters are not selected properly, the second-order spring damping system composed of tool-workpiece will chatter due to the regeneration effect. The modal parameters of the tool-workpiece system have a great

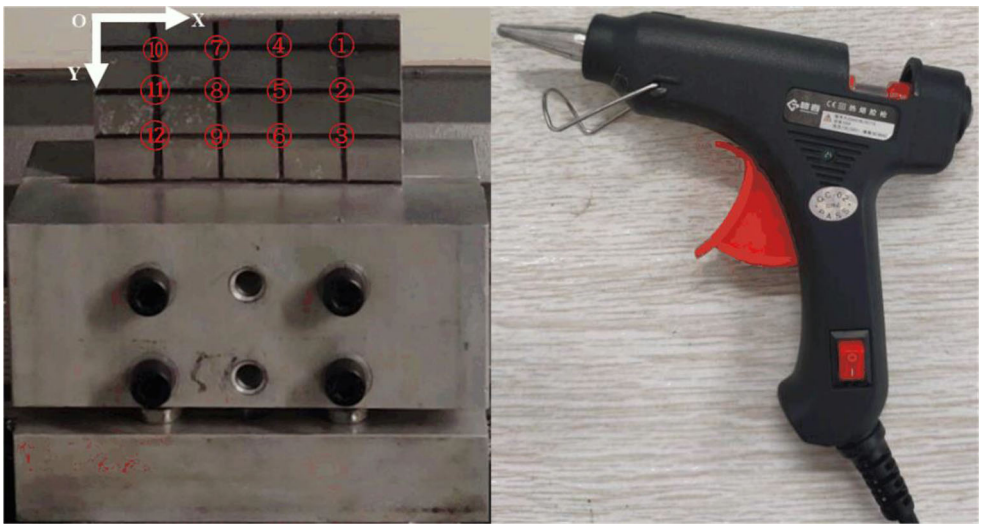

Fig. 4 Experimental equipment and materials: **a** thin-walled part and **b** glue gun

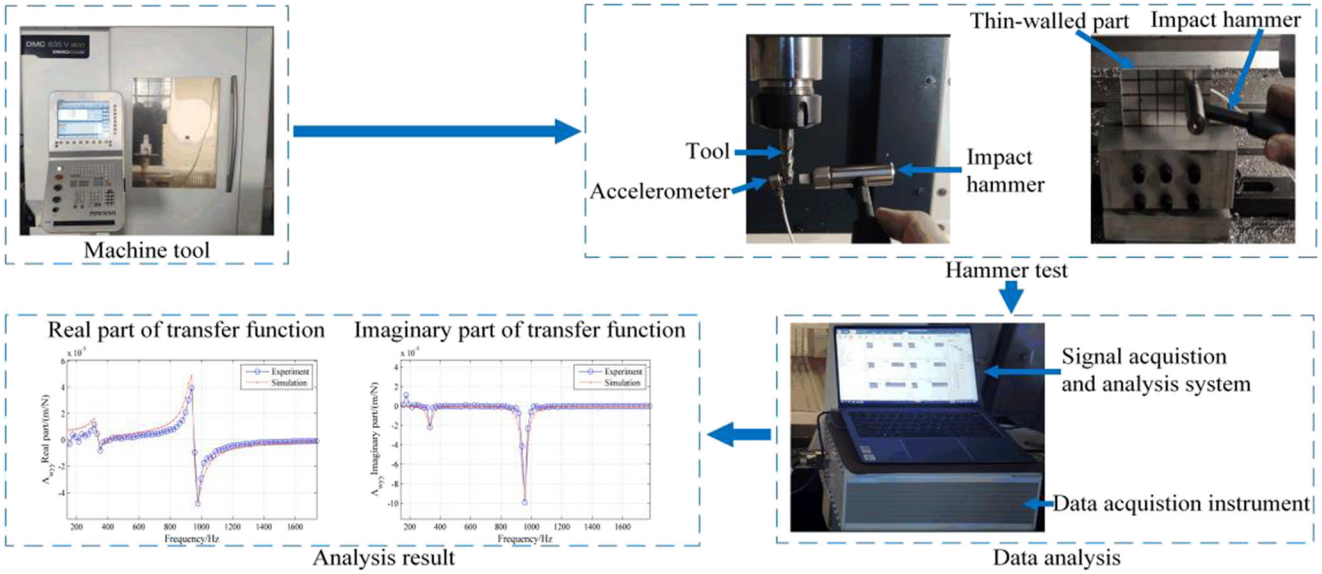

Fig. 5 Device and process of the modal experiment

Table 1 Modal parameter identification results

Modal orders	Natural frequency (Hz)	Stiffness (N/m)	Damping ratio (%)
Workpiece point 1 y direction 1st	332	3.6163×10^{5}	5.89
Workpiece point 1 y direction 2nd	976.6	3.7464×10^{5}	2.00
Workpiece point 2 y direction 1st	332	5.0392×10^{5}	5.89
Workpiece point 2 y direction 2nd	1007	4.1786×10^{6}	0.99
Workpiece point 3 y direction 1st	332	8.1645×10^{5}	5.89
Workpiece point 3 y direction 2nd	1005	2.8826×10^{7}	0.99
Workpiece point 4 y direction 1st	332	4.8026×10^{5}	5.89
Workpiece point 4 y direction 2nd	965.4	1.0549×10^{6}	1.02
Workpiece point 5 y direction 1st	332	4.9252×10^{5}	5.89
Workpiece point 5 y direction 2nd	1003	4.9364×10^{5}	1.96
Workpiece point 6 y direction 1st	332	6.8865×10^{5}	5.89
Workpiece point 6 y direction 2nd	1005	7.3235×10^{6}	0.99
Workpiece point 7 y direction 1st	332	3.9057×10^{5}	5.89
Workpiece point 7 y direction 2nd	953.1	2.4590×10^{5}	2.05
Workpiece point 8 y direction 1st	332	5.0906×10^{5}	5.89
Workpiece point 8 y direction 2nd	1005	7.6576×10^{5}	1.96
Workpiece point 9 y direction 1st	332	7.7051×10^{5}	5.89
Workpiece point 9 y direction 2nd	1005	7.2613×10^{6}	0.99
Workpiece point 10 y direction 1st	332	4.4041×10^{5}	5.89
Workpiece point 10 y direction 2nd	932.8	6.9147×10^{5}	2.09
Workpiece point 11 y direction 1st	332	4.4041×10^{5}	5.89
Workpiece point 11 y direction 2nd	989.6	7.2613×10^{5}	1.99
Workpiece point 12 y direction 1st	332	6.6027×10^{5}	5.89
Workpiece point 12 y direction 2nd	1005	9.2580×10^{6}	0.99
Tool x direction 1st	1484	1.0268×10^{7}	5.93
Tool x direction 2nd	3450	1.2181×10^{7}	1.42
Tool y direction 1st	1592	1.1085×10^{7}	7.98
Tool y direction 2nd	3413	1.5353×10^{7}	2.86

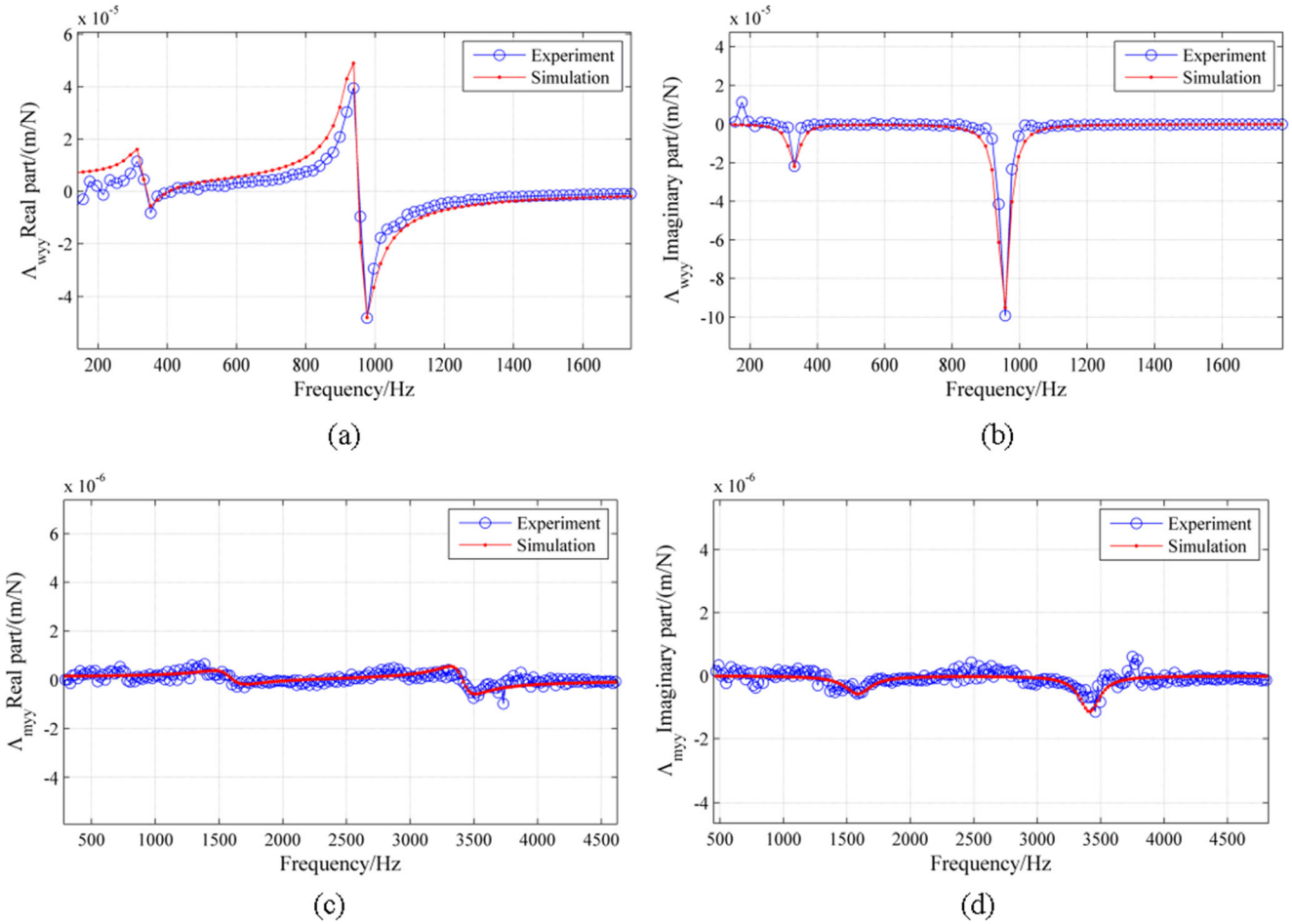

Fig. 6 Transfer function curves of tool and workpiece: **a** Re of TF of the workpiece point 7, **b** Im of TF of the workpiece point 7, **c** Re of TF of the tool, and **d** Im of TF of the tool

influence on the machining stability. By obtaining the modal of the process system, the stability equation of the system can be obtained, and the stability boundary can be further solved. Therefore, it is necessary to conduct modal experiment and modal analysis. The modal experiment aims to obtain the modal parameters (natural frequency, stiffness, and damping ratio) of the tool and the workpiece.

3.1 Relative transfer function

The relative vibration of the tool and the workpiece will directly affect the machining accuracy of the workpiece surface. Different from general processing, the thin-walled parts have a thinner wall thickness, and the relative deformation generated during the processing is relatively large. So, it is necessary to consider the modal of the workpiece to improve accuracy. Therefore, for the tool-workpiece second-order spring damping system where the workpiece is a thin-walled part, not only the vibration of the tool but also the vibration of the workpiece must be considered, as shown in Fig. 2.

For a 2 DOF milling system for thin-walled parts, it can be expressed as:

$$\begin{cases} \ddot{x} + 2\zeta_x\omega_{n,x}\dot{x} + \omega_{n,x}^2 x = \dfrac{1}{m_x}F_x(x) \\ \ddot{y} + 2\zeta_y\omega_{n,y}\dot{y} + \omega_{n,y}^2 y = \dfrac{1}{m_y}F_y(y) \end{cases} \quad (26)$$

In Eq. (26), ζ_x and ζ_y are the damping ratio of the system in the x and y directions, respectively, and $\omega_{n,x}$ and $\omega_{n,y}$ are the natural frequencies of the system in the x and y directions, respectively. After Laplace transform, Eq. (26) can be transformed into:

$$\begin{cases} \left(s^2 + 2\zeta_x\omega_{n,x}s + \omega_{n,x}^2\right)x(s) = \dfrac{1}{m_x}F_x(s) \\ \left(s^2 + 2\zeta_y\omega_{n,y}s + \omega_{n,y}^2\right)y(s) = \dfrac{1}{m_y}F_y(s) \end{cases} \quad (27)$$

In Eq. (27), the forces $F_x(s)$ and $F_y(s)$ in the x and y directions are the input of the system, and the displacements $x(s)$ and $y(s)$ in the x and y directions are the output of the system. Therefore, the transfer function of a 2 DOF system can be obtained:

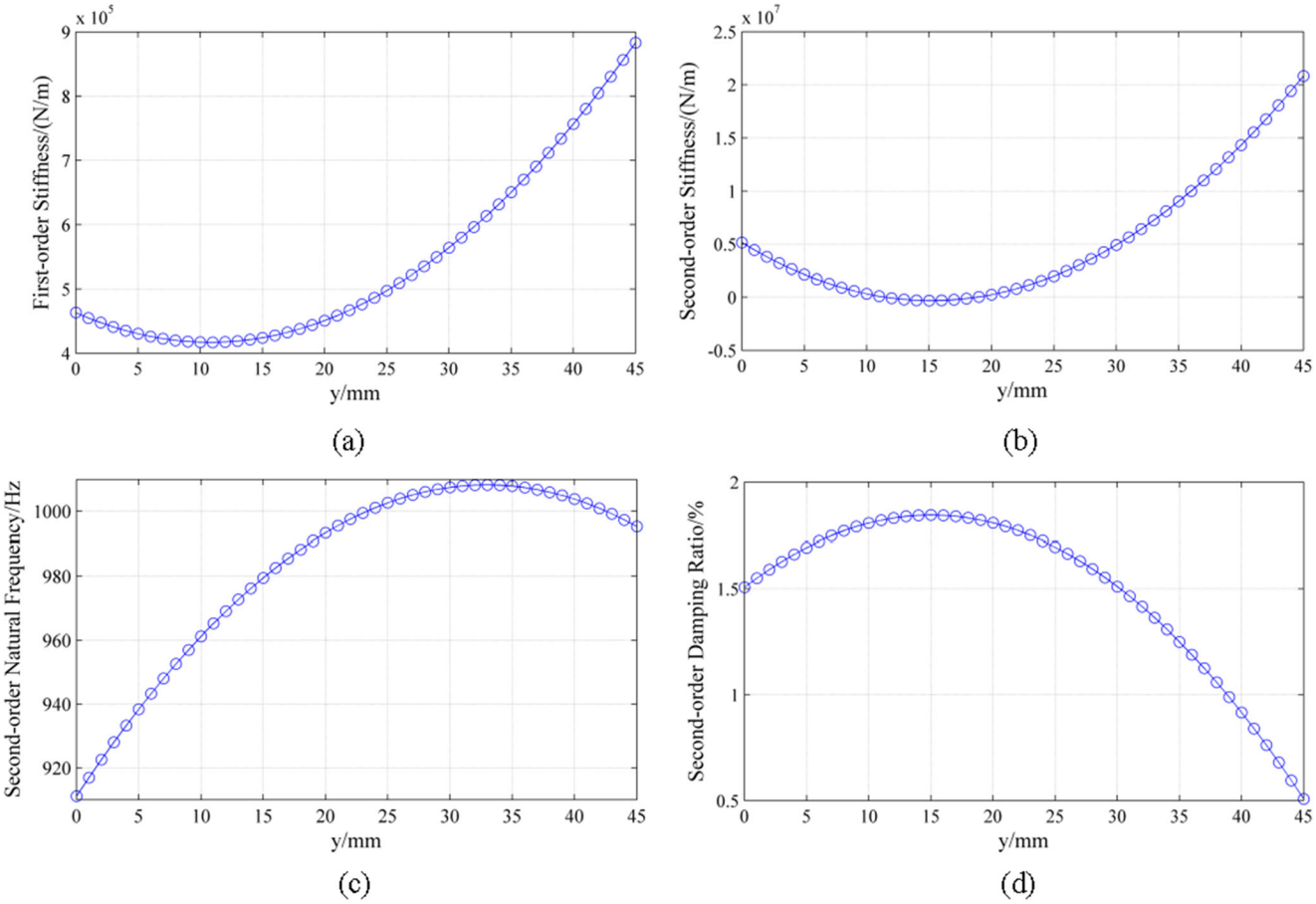

Fig. 7 Modal parameter fitting curve of workpiece: **a** first-order stiffness, **b** second-order stiffness, **c** second-order natural frequency, and **d** second-order damping ratio

$$\begin{cases} \Lambda_x(s) = \dfrac{x(s)}{F_x(s)} = \dfrac{\omega_{n,x}^2}{k_x\left(s^2 + 2\xi_x\omega_{n,x} + \omega_{n,x}^2\right)} \\ \Lambda_y(s) = \dfrac{y(s)}{F_y(s)} = \dfrac{\omega_{n,y}^2}{k_y\left(s^2 + 2\xi_y\omega_{n,y} + \omega_{n,y}^2\right)} \end{cases} \tag{28}$$

As shown in Fig. 3, the feed directions of down-milling and up-milling are different. No matter under up-milling or down-milling, the force of the workpiece is equal to the force of the tool, and the direction is opposite. The relative displacement in the y direction of both down-milling and up-milling can be expressed as the sum of the displacement of the tool and the workpiece:

$$\begin{cases} \Delta_{relative(xx)} = \Delta_{cutter(xx)} \\ \Delta_{relative(yy)} = \Delta_{cutter(yy)} + \Delta_{workpiece(yy)} \end{cases} \tag{29}$$

Table 2 Modal parameters used in simulation

Modal orders	Natural frequency (Hz)	Stiffness (N/m)	Damping ratio (%)
Workpiece y direction 1st	332	4.632×10^5	10.61
Workpiece y direction 2nd	911.1	5.147×10^6	15.70
Tool x direction 1st	1484	1.0268×10^7	5.93
Tool x direction 2nd	3450	1.2181×10^7	1.42
Tool y direction 1st	1592	1.1085×10^7	7.98
Tool y direction 2nd	3413	1.5353×10^7	2.86

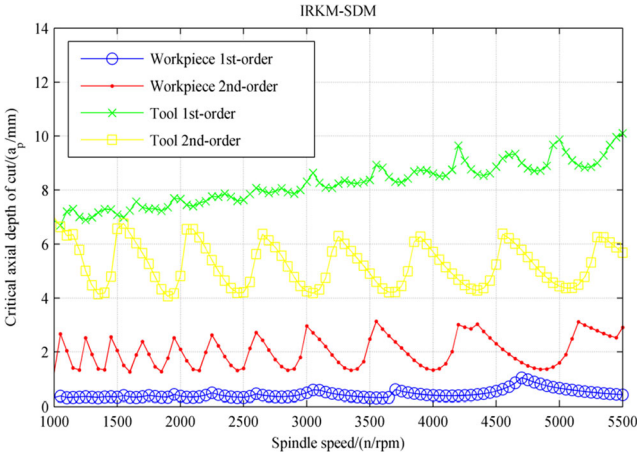

Fig. 8 Chatter stability lobe diagrams under different modal parameters

Furthermore, the transfer function can be obtained as:

$$\begin{cases} \Lambda_{relative(xx)} = \dfrac{\Delta_{relative(xx)}}{F_{relative(xx)}} = \dfrac{\Delta_{cutter(xx)}}{F_x} \\ \Lambda_{relative(yy)} = \dfrac{\Delta_{relative(yy)}}{F_{relative(yy)}} = \dfrac{\Delta_{cutter(yy)}}{F_{cutter(yy)}} + \dfrac{\Delta_{workpiece(yy)}}{F_{workpiece(yy)}} = \dfrac{\Delta_{cutter(yy)} + \Delta_{workpiece(yy)}}{F_y} \end{cases} \tag{30}$$

Since the transfer function of each order mode of the system in the same direction can be superimposed, the relative transfer function of the 2 DOF system with the q-order mode of the tool and the w-order mode of the workpiece can be expressed as:

$$\begin{cases} \Lambda_{relative(xx)} = \sum_{i=1}^{q} \Lambda^i_{cutter(xx)} \\ \Lambda_{relative(yy)} = \sum_{i=1}^{q} \Lambda^i_{cutter(yy)} + \sum_{i=1}^{w} \Lambda^i_{workpiece(yy)} \end{cases} \tag{31}$$

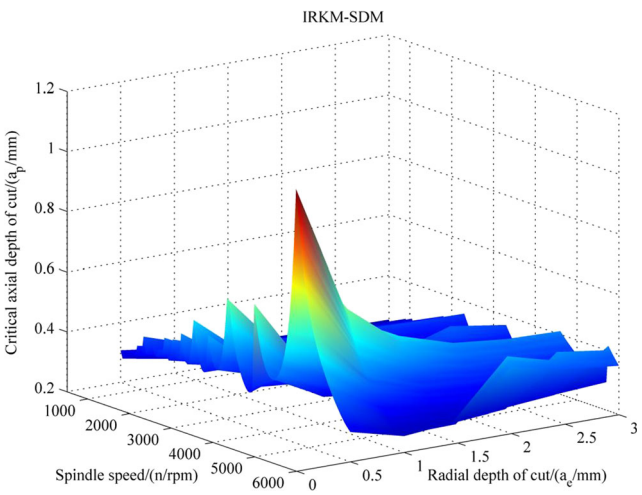

Fig. 9 Three-dimensional stability lobe diagram based on IRKM-SDM

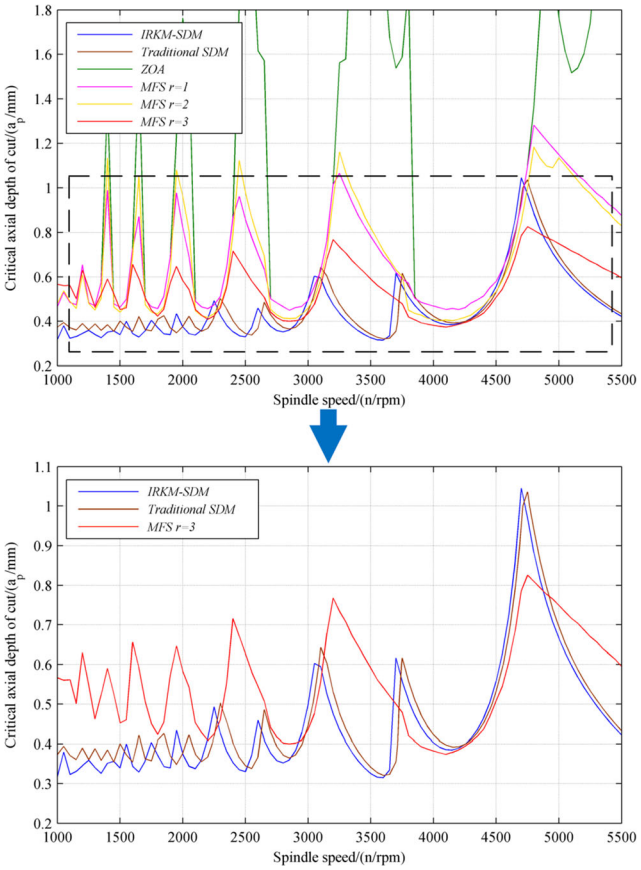

Fig. 10 Stability lobe diagram comparison of different algorithms

3.2 Tool-workpiece modal experiment and analysis

In order to obtain the required modal parameters, the method of hammer experiment is used to analyze the modal. The principle of the hammer experiment is to generate a force with a short duration by hammering the object to obtain the displacement response. By analyzing the force and displacement generated by the hammering, the frequency response function can be obtained, and the modal parameters can be further obtained.

The instrument used in the experiment are as follows: the impact hammer is Kistler 9722A500, the accelerometer is Kistler 8776B050A, the data acquisition card is the 5922D dynamic signal acquisition card, and the data acquisition software is the DHDAS dynamic signal acquisition and analysis system. The hammering objects are integral alloy milling cutter MAL-2E-10 (overhang length is 45mm) and aluminum alloy (6061T6) thin-walled parts (size 100×120×5mm^3). Because the natural frequency and stiffness of each position of the workpiece are different, this experiment selects twelve test points on the workpiece, takes the average of the obtained modal parameters, and performs curve fitting, so as to obtain the modal parameters of each position in the y direction. The accelerometer is glued to the tool and the back of the measuring points of the workpiece through a 50-W glue gun. The

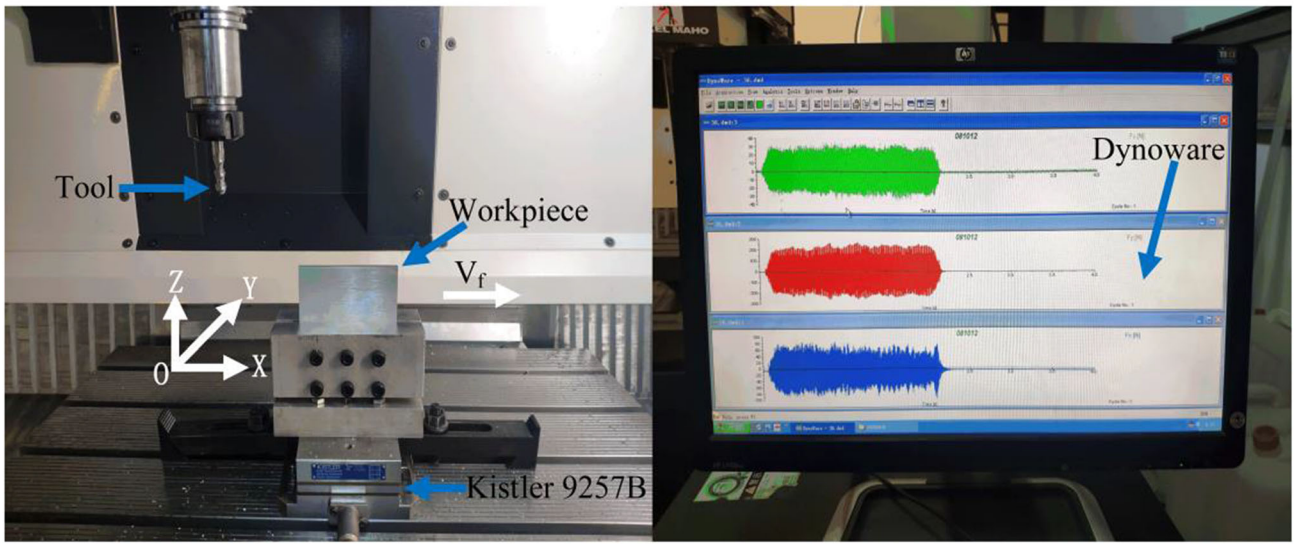

Fig. 11 Stability verification experimental platform

position of the measuring points on the workpiece and the glue gun used are shown in Fig. 4.

The device and process of the modal experiment are shown in Fig. 5.

The modal parameters of the tool and workpiece obtained from the modal experiment are shown in Table 1.

In order to verify the accuracy of the modal parameters obtained by the experiment, curve fitting of transfer function is performed on the identified modal parameters, and some fitting results are shown in Fig. 6. Figure 6 a and b are the real and imaginary part curves of the transfer function (TF) of the workpiece point 7 in

Table 3 Stability verification experiment parameters

Serial number	Spindle speed/rpm	Axial depth of cut/mm	Radial depth of cut/mm	Feed rate /(mm/z)
1	1500	0.5	0.5	0.1
2	1500	0.4	0.5	0.1
3	1500	0.3	0.5	0.1
4	2000	0.5	0.5	0.1
5	2000	0.4	0.5	0.1
6	2000	0.3	0.5	0.1
7	2250	0.6	0.5	0.1
8	2250	0.5	0.5	0.1
9	2250	0.4	0.5	0.1
10	2500	0.5	0.5	0.1
11	2500	0.4	0.5	0.1
12	2500	0.3	0.5	0.1
13	3100	0.7	0.5	0.1
14	3100	0.6	0.5	0.1
15	3100	0.5	0.5	0.1
16	3500	0.5	0.5	0.1
17	3500	0.4	0.5	0.1
18	3500	0.3	0.5	0.1
19	4000	0.5	0.5	0.1
20	4000	0.4	0.5	0.1
21	4000	0.3	0.5	0.1
22	4500	0.7	0.5	0.1
23	4500	0.6	0.5	0.1
24	4500	0.5	0.5	0.1
25	4700	1.1	0.5	0.1
26	4700	1.0	0.5	0.1
27	4700	0.9	0.5	0.1
28	5000	0.8	0.5	0.1
29	5000	0.7	0.5	0.1
30	5000	0.6	0.5	0.1

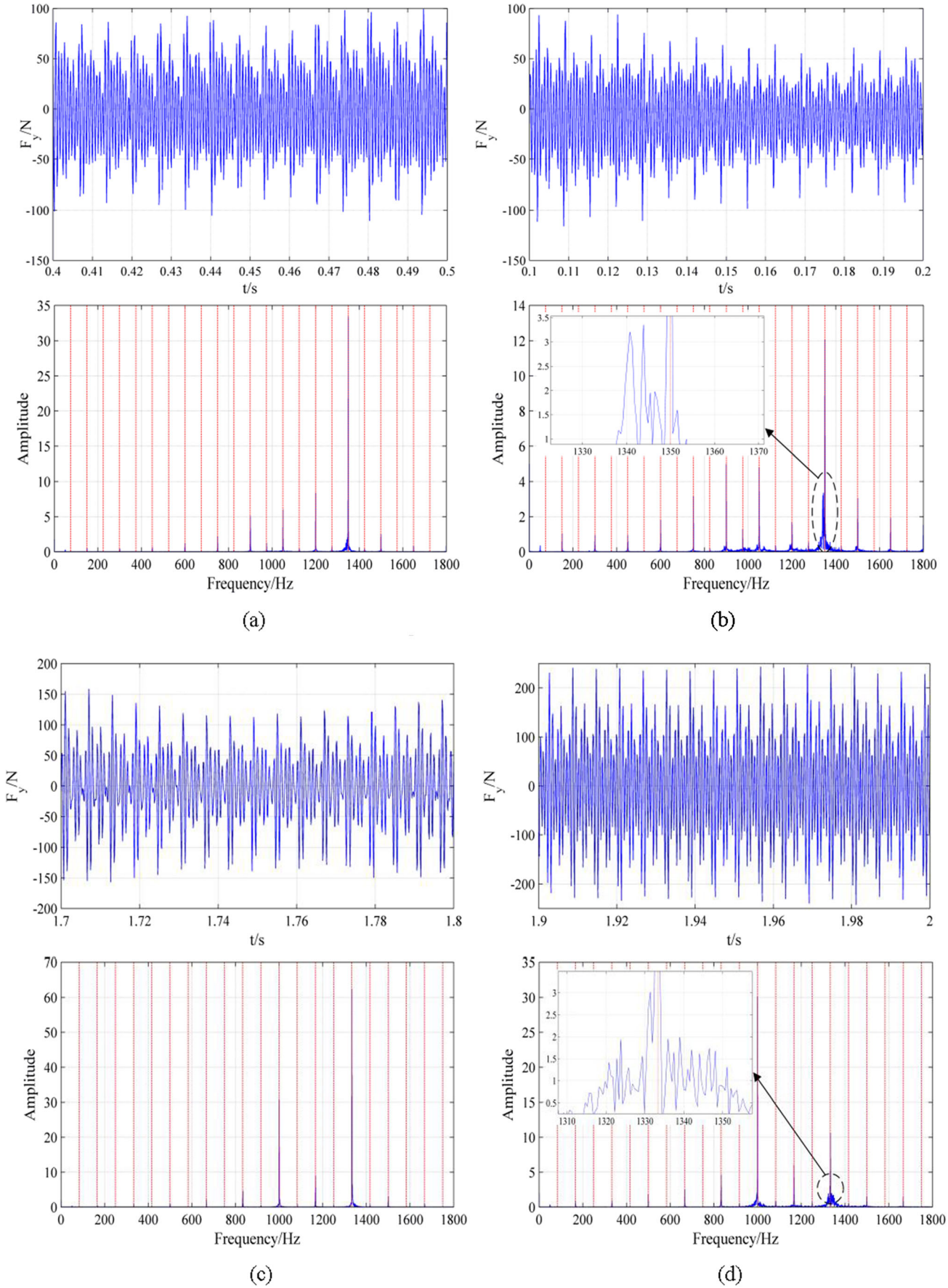

Fig. 12 Time domain and frequency domain waveforms of cutting force: **a** n=4500rpm, a_p=0.5mm, **b** n=4500rpm, a_p=0.7mm, **c** n=5000rpm, a_p=0.6mm, and **d** n=5000rpm, a_p=0.8mm

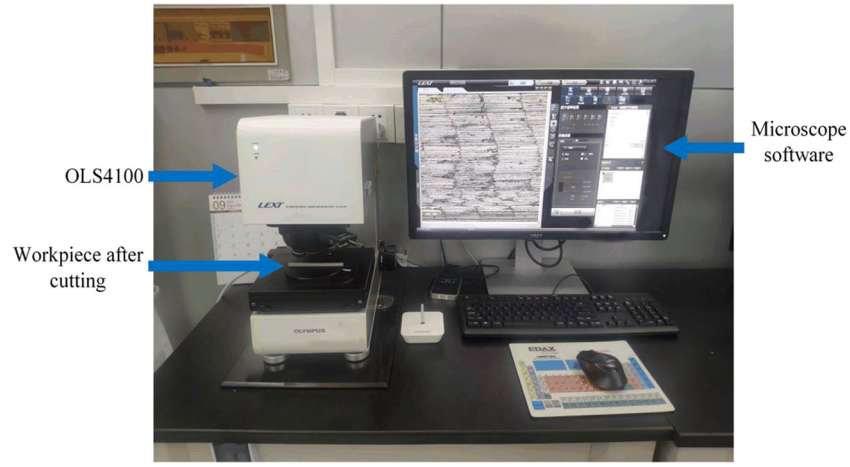

Fig. 13 Laser measuring microscope experimental platform

the y direction, and Fig. 6 c and d are the real and imaginary part curves of the transfer function (TF) of the tool in the y direction, respectively. It can be seen from Fig. 6 that the fitted curves have good consistency with the experimental curves. Therefore, the identified parameters are basically accurate.

The workpiece coordinate system setting is shown in Fig. 4a. The modal parameters obtained from 12 measuring points of the workpiece are averaged in the x direction, and then the obtained average of the x direction are fitted by quadratic polynomial in the y direction to obtain the modal parameter curve of the workpiece in the y direction. The curves obtained are shown in Fig. 7.

The formula of fitting curve in Fig. 7 is as follows:

$$\begin{cases} (a): fos = 398.1y^2 - 8582y + 4.632e5(N/m) \\ (b): sos = 2.373e4y^2 - 7197e5y + 5.147e6(N/m) \\ (c): sonf = -0.08961y^2 + 5.902y + 911.1(Hz) \\ (d): sodr = 2.373e(-3)y^2 - 0.0448y + 1.507(\%) \end{cases} \quad (32)$$

4 Chatter stability analysis of thin-walled parts based on the IRKM-SDM

4.1 Lobe diagram simulation of chatter stability of thin-walled parts

According to the fitting curve obtained in Fig. 7, the modal parameters at the top of the workpiece are taken as the modal parameters for simulation. The modal parameters used in the simulation are shown in Table 2.

Other parameters for simulation are as follows: number of tool teeth $N = 2$, tool diameter $d = 10mm$, the tangential cutting force coefficient is $K_t = 25.8724 \times 10^6 (N/m^2)$, and the radial cutting coefficient is $K_r = -7.66466 \times 10^8 (N/m^2)$. Choose down-milling as the milling method and determine the discretization number $m = 44$ of the period T, the minimum spindle speed $n_{\min} = 500$ (rpm), the maximum spindle speed $n_{\max} = 6000$ (rpm), the maximum axial depth of cut $a_{p\max} = 100(mm)$, the minimum axial depth of cut difference $c = 5 \times 10^{-7} mm$, the definite integral discrete interval number $int\_k = 100$, and spindle speed discrete number $stx = 110$. The modal parameters are shown in the table. The first-order modal mass of the thin-walled part is $m_{wt1} = 0.1061kg$, the second-

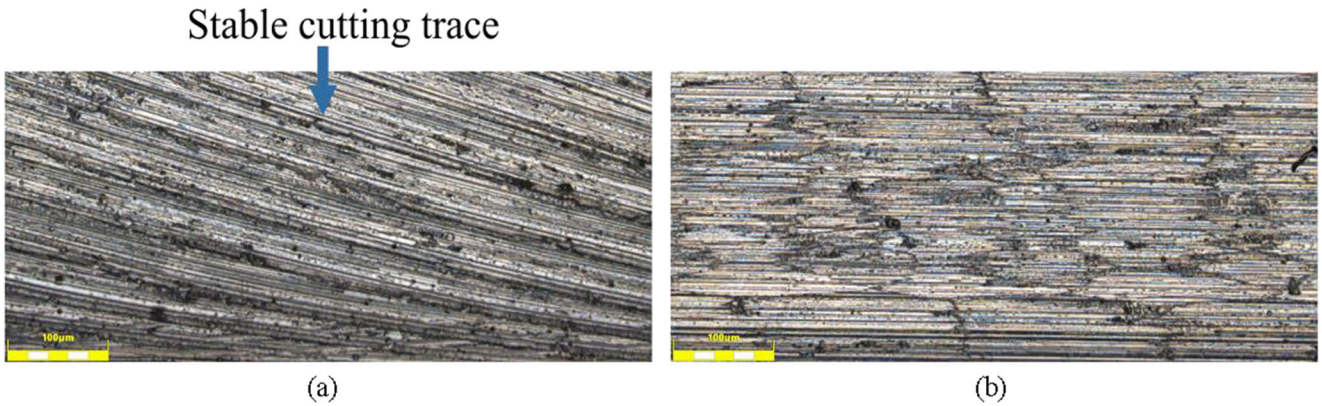

Fig. 14 Micro machined surface: **a** $n = 5000rpm$, $a_p = 0.6mm$ and **b** $n = 5000rpm$, $a_p = 0.8mm$

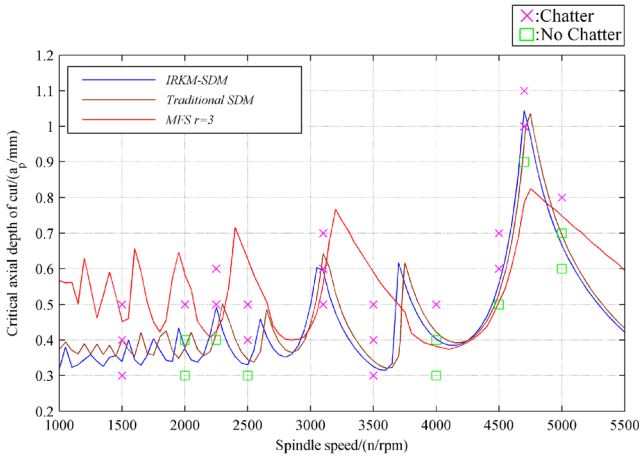

Fig. 15 Stability lobe diagram of cutting experiment

order modal mass of the thin-walled part is $m_{wt2} = 0.1570kg$, the first-order modal mass of the tool is $m_{mt1} = 0.1177kg$, and the second-order modal mass of the tool is $m_{mt2} = 0.0259kg$.

The IRKM-SDM is used to draw the lobe diagram, and the radial depth of cut $a_e = 0.5mm$ is taken to obtain the lobe diagram under different modal parameters, as shown in Fig. 8. Taking the lowest critical depth of cut at the same speed as the critical axial depth of milling, the chatter stability lobe diagram of the milling system can be obtained.

Select the radial depth of cut $a_e = 0.5mm$, $1.0mm$, $1.5mm$, $2.0mm$, $2.5mm$, and $3.0mm$. The first-order and second-order modal parameters of the tool and the workpiece are coupled, and the simulated three-dimensional lobe diagram is shown in Fig. 9. It can be seen from Fig. 9 that as the radial depth of cut gradually increases, the critical axial depth of cut gradually decreases, which is consistent with the actual situation.

In order to verify the IRKM-SDM, take the radial depth of cut $a_e = 0.5mm$ and compare the IRKM-SDM with the ZOA, MFS, and traditional SDM. The simulated lobe diagram is shown in Fig. 10.

It can be seen from Fig. 10 that the trends of the lobe diagrams simulated by different methods are different. The lobe diagram simulated by the IRKM-SDM is similar in value and trend to the traditional SDM method and MFS (directional coefficient is 3), but it is far different from the ZOA and MFS (directional coefficient is 1 or 2). Therefore, it is necessary to verify the method of this paper through milling experiments.

4.2 Verification of the chatter stability of the IRKM-SDM

This verification experiment uses the tools and aluminum alloy thin-walled parts used in the previous modal experiments, and the tool overhang length is maintained at 45mm, which is consistent with the previous modal experiments. The experiment uses the dynamometer Kistler 9257B and the mechanical analysis software DynoWare to collect the force signal and applies the fast Fourier transform to analyze the force signal to determine whether chatter occurs. The construction of the experimental platform is shown in Fig. 11.

According to the simulation results, each set of experiments will start cutting from the top of each workpiece. The experiment parameters are shown in Table 3.

Figure 12 shows the time domain diagram and frequency domain diagram of the force signal in the y direction measured by the experiment. When the spindle speed is 4500rpm, the base frequency is 4500/60Hz; when the spindle speed is 5000rpm, the base frequency is 5000/60Hz. The base frequency and its integer multiples are shown in red dotted lines in Fig. 12. If there is a frequency close to but not equal to the frequency of the main structure of the machining system in the force spectrum, it indicates that chatter has occurred during the milling process [29]. It can be seen from Fig. 12 a and c that there is no chatter frequency at this time; and from the black circle in Fig. 12 b and d, it can be seen that at this time, an obvious unknown frequency appears at the position close to

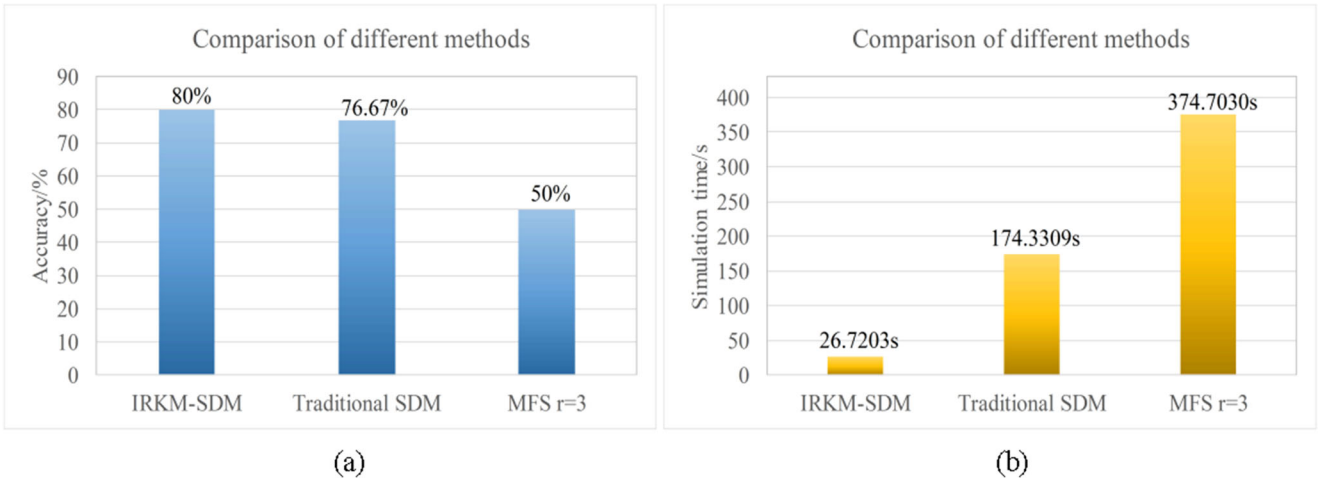

Fig. 16 Comparison results of different methods: **a** accuracy and **b** simulation time

the integral multiple of the base frequency of the spindle, so it can be judged that chatter occurs at this time.

In order to further verify whether chatter vibration occurs, after cutting the processed workpiece, use a 3D measuring laser microscope for surface observation. The model of the laser microscope is OLS4100, and the experimental equipment is shown in Fig. 13. The observed surface topography is shown in Fig. 14.

It can be seen from Fig. 14a that when chatter does not occur, a stable cutting trace can be observed from the surface of the workpiece, and the overall surface is relatively smooth. And as can be seen from Fig. 14b, the surface of the workpiece with chatter is obviously different from the surface of the workpiece without chatter. On the surface of the workpiece with chatter, no stable cutting trace can be observed, and the surface is relatively rough.

According to the final experimental results, the lobe diagrams simulated by different methods are compared in terms of simulation accuracy and calculation speed. Since the simulation results of the ZOA and the MFS (directional coefficient is 1 or 2) are far from those of other methods, only the IRKM-SDM, the traditional SDM, and the MFS (directional coefficient is 3) are compared here. The final experimental results are shown in Fig. 15, and the comparison results of different methods are shown in Fig. 16.

It can be seen from Fig. 16 that the IRKM-SDM is higher than other methods in terms of simulation accuracy and calculation speed. It is worth noting that due to the small critical axial depth of cut obtained by the simulation, some of the selected experimental parameters are very close to the critical axial depth of cut, as shown in point A (4700, 1. 0) and point B (5000, 0. 7) in Fig. 15. Therefore, at these points, the inconsistency between the experimental results and the simulation results is a normal error.

5 Conclusion

In this paper, the semi-discretization method based on the improved Runge-Kutta method (IRKM-SDM) is used to predict the milling stability. The aluminum alloy thin-walled parts are taken as the research object. The modal parameters of the tool and the workpiece are obtained through modal analysis. After coupling the parameters of the workpiece and the cutter, the chatter stability lobe diagram is obtained, which is verified by milling experiments. According to theoretical analysis, simulation, and experimental results, the conclusions are as follows:

(1) The modal parameters of each position of the thin-walled part are different. The modal parameters obtained from different measuring points of the workpiece are averaged in the x direction, and the obtained average of the x direction is fitted in the y direction by a quadratic polynomial to obtain the modal parameters of each position of the workpiece in the y direction.
(2) Chatter is prone to occur when machining thin-walled parts. As the radial depth of cut increases, the critical axial depth of cut gradually decreases. Therefore, in order to ensure the stability during processing, it is necessary to control the axial depth of cut.
(3) In the milling system, the lobe diagrams obtained by the modal parameters of the workpiece and the tool are different. Therefore, in order to ensure the accuracy of the lobe diagram, it is necessary to couple the modal parameters of the workpiece and the tool.
(4) According to the results of simulation and experiment, compared with other methods, the simulation accuracy of the lobe diagram simulated by the IRKM-SDM is 80%, and the calculation time is only 26. 72032s. In comparison, the simulation accuracy of the traditional SDM is 76. 67%, and the calculation time is 174. 3309s; the simulation accuracy of the MFS (directional coefficient is 3) is 50%, and the calculation time is 374. 7030s. Therefore, considering the simulation accuracy and calculation speed comprehensively, in the processing of thin-walled parts, the IRKM-SDM has advantages over the ZOA, the MFS, and the traditional SDM.

Nomenclature ω_n, The natural frequency of the system; ζ, The damping ratio; m_t, The modal mass; a_p, The axial depth of cut; $h(t)$, The projection of the specific cutting force coefficient; K_t, The tangential cutting force coefficient; K_n, The radial cutting force coefficient; $\phi_j(t)$, The contact angle of the jth tooth; n, The spindle speed; ϕ_p, The angle between the cutter teeth; N, The number of cutter teeth; $g(\phi_j)$, The unit step function; ϕ_{st},ϕ_{ex}, The contact angles when the tool is cut in and out, respectively; a_e, The radial depth of cut; D, The tool diameter; $A(t)$,$B(t)$, The periodic matrices; T, The time period; τ, The angular frequency of the spindle; Δt, The time step; m, The discretization number of time; Φ, The conversion matrix; c, The minimum axial depth of cut difference; int _ k, The definite integral discrete interval number; F_x,F_y, The forces in the x and y directions; Λ, The transfer function; Δ, The relative displacement; *fos*, The first-order stiffness; *sos*, The second-order stiffness; *sonf*, The second-order natural frequency; *sodr*, The second-order damping ratio

Availability of data and materials The data that support the findings of this study are available from the corresponding author upon reasonable request.

Author contribution Muxuan Guo and Lida Zhu conceived the idea. Muxuan Guo and Boling Yan performed all the experiments. Muxuan Guo drafted the manuscript, and Muxuan Guo, Lida Zhu, Boling Yan, and Zhihong Guan interpreted, discussed, and edited the manuscript. Muxuan Guo and Zhihong Guan finalized the manuscript, including preparing the detailed response letter. Lida Zhu supervised the work.

Funding This work was supported by the National Natural Science Foundation of China (51975112) and Fundamental Research Funds for Central Universities (N180305032) and supported by Liao Ning Revitalization Talents Program (XLYC1807063).

Declarations

Ethics approval Not applicable.

Consent to participate Not applicable.

Consent for publication The manuscript is approved by all authors for publication. I would like to declare on behalf of my co-authors that the work described was original research that has not been published previously, and not under consideration for publication elsewhere, in whole or in part.

Competing interests The authors declare no competing interests.

References

1. Totis G, Sortino M (2020) Polynomial Chaos-Kriging approaches for an efficient probabilistic chatter prediction in milling. Int J Mach Tools Manuf 157:103610. https://doi.org/10.1016/j.ijmachtools.2020.103610
2. Yang Z, Zhu L, Zhang G, Ni C, Lin B (2020) Review of ultrasonic vibration-assisted machining in advanced materials. International. Journal of Machine Tools and Manufacture 156:103594. https://doi.org/10.1016/j.ijmachtools.2020.103594
3. Altintaş Y, Budak E (1995) Analytical prediction of stability lobes in milling. CIRP Ann 44(1):357–362. https://doi.org/10.1016/s0007-8506(07)62342-7
4. Bayly PV, Mann BP, Schmitz TL, Peters DA, Stepan G, Insperger T (2002) Effects of radial immersion and cutting direction on chatter instability in end-milling. In: ASME International Mechanical Engineering Congress and Exposition:351–363. https://doi.org/10.1115/imece2002-39116
5. Merdol SD, Altintas Y (2004) Multi frequency solution of chatter stability for low immersion milling. J Manuf Sci Eng 126(3):459–466. https://doi.org/10.1115/1.1765139
6. Insperger T, Stépán G (2002) Semi-discretization method for delayed systems. Int J Numer Methods Eng 55(5):503–518. https://doi.org/10.1002/nme.505
7. Insperger T, Stépán G (2004) Updated semi-discretization method for periodic delay-differential equations with discrete delay. Int J Numer Methods Eng 61(1):117–141. https://doi.org/10.1002/nme.1061
8. Ding Y, Zhu L, Zhang X, Ding H (2010) A full-discretization method for prediction of milling stability. Int J Mach Tools Manuf 50(5):502–509. https://doi.org/10.1016/j.ijmachtools.2010.01.003
9. Ding Y, Zhu L, Zhang X, Ding H (2010) Second-order full-discretization method for milling stability prediction. Int J Mach Tools Manuf 50(10):926–932. https://doi.org/10.1016/j.ijmachtools.2010.05.005
10. Li Z, Sun Y, Guo D (2016) Chatter prediction utilizing stability lobes with process damping in finish milling of titanium alloy thin-walled workpiece. Int J Adv Manuf Technol 89(9-12):2663–2674. https://doi.org/10.1007/s00170-016-9834-3
11. Liu B, Zhu L, Dun Y, Liu C (2016) Investigation on chatter stability of thin-walled parts in milling based on process damping with relative transfer functions. Int J Adv Manuf Technol 89(9-12):2701–2711. https://doi.org/10.1007/s00170-016-9431-5
12. Wu S, Li R, Liu X, Yang L, Zhu M (2016) Experimental study of thin wall milling chatter stability nonlinear criterion. Procedia CIRP 56:422–427. https://doi.org/10.1016/j.procir.2016.10.075
13. Ma Y, Wan M, Zhang W (2016) Effect of cutter runout on chatter stability of milling process. Procedia CIRP 56:115–118. https://doi.org/10.1016/j.procir.2016.10.034
14. Zhang X, Xiong C, Ding Y, Ding H (2016) Prediction of chatter stability in high speed milling using the numerical differentiation method. Int J Adv Manuf Technol 89(9-12):2535–2544. https://doi.org/10.1007/s00170-016-8708-z
15. Ozoegwu CG, Ofochebe SM, Omenyi SN (2016) A method of improving chatter-free conditions with combined-mode milling. J Manuf Process 21:1–13. https://doi.org/10.1016/j.jmapro.2015.10.008
16. Comak A, Budak E (2017) Modeling dynamics and stability of variable pitch and helix milling tools for development of a design method to maximize chatter stability. Precis Eng 47:459–468. https://doi.org/10.1016/j.precisioneng.2016.09.021
17. Hajdu D, Insperger T, Bachrathy D, Stepan G (2017) Prediction of robust stability boundaries for milling operations with extended multi-frequency solution and structured singular values. J Manuf Process 30:281–289. https://doi.org/10.1016/j.jmapro.2017.09.015
18. Jiang S, Sun Y, Yuan X, Liu W (2017) A second-order semi-discretization method for the efficient and accurate stability prediction of milling process. Int J Adv Manuf Technol 92(1-4):583–595. https://doi.org/10.1007/s00170-017-0171-y
19. Jafarzadeh E, Movahhedy MR (2017) Numerical simulation of interaction of mode-coupling and regenerative chatter in machining. J Manuf Process 27:252–260. https://doi.org/10.1016/j.jmapro.2017.05.008
20. Dai Y, Li H, Xing X, Hao B (2018) Prediction of chatter stability for milling process using precise integration method. Precis Eng 52:152–157. https://doi.org/10.1016/j.precisioneng.2017.12.003
21. Dai Y, Li H, Wei Z, Zhang H (2018) Chatter stability prediction for five-axis ball end milling with precise integration method. J Manuf Process 32:20–31. https://doi.org/10.1016/j.jmapro.2018.01.008
22. Liu C, Zhu L, Ni C (2018) Chatter detection in milling process based on VMD and energy entropy. Mech Syst Signal Process 105:169–182. https://doi.org/10.1016/j.ymssp.2017.11.046
23. Zhu L, Liu C (2020) Recent progress of chatter prediction, detection and suppression in milling. Mech Syst Signal Process 143:106840. https://doi.org/10.1016/j.ymssp.2020.106840
24. Sun Y, Jiang S (2018) Predictive modeling of chatter stability considering force-induced deformation effect in milling thin-walled parts. Int J Mach Tools Manuf 135:38–52. https://doi.org/10.1016/j.ijmachtools.2018.08.003
25. Zhou K, Zhang J, Xu C, Feng P, Wu Z (2018) Effects of helix angle and multi-mode on the milling stability prediction using full-discretization method. Precis Eng 54:39–50. https://doi.org/10.1016/j.precisioneng.2018.04.016
26. Kiss AK, Hajdu D, Bachrathy D, Stepan G (2018) Operational stability prediction in milling based on impact tests. Mech Syst Signal Process 103:327–339. https://doi.org/10.1016/j.ymssp.2017.10.019
27. Wan S, Jin X, Maroju NK, Hong J (2019) Effect of vibration assistance on chatter stability in milling. Int J Mach Tools Manuf 145:103432. https://doi.org/10.1016/j.ijmachtools.2019.103432
28. Yang Y, Zhang W-H, Ma Y-C, Wan M, Dang X-B (2019) An efficient decomposition-condensation method for chatter prediction in milling large-scale thin-walled structures. Mech Syst Signal Process 121:58–76. https://doi.org/10.1016/j.ymssp.2018.11.013
29. Dun Y, Zhu L, Wang S (2020) Multi-modal method for chatter stability prediction and control in milling of thin-walled workpiece. Appl Math Model 80:602–624. https://doi.org/10.1016/j.apm.2019.12.003
30. Chen Q, Li W, Ren Y, Zhou Z (2020) 3D chatter stability of high-speed micromilling by considering nonlinear cutting coefficients, and process damping. J Manuf Process 57:552–565. https://doi.org/10.1016/j.jmapro.2020.07.016

31. Niu J, Ding Y, Zhu L, Ding H (2013) Runge–Kutta methods for a semi-analytical prediction of milling stability. Nonlinear Dynamics 76(1):289–304. https://doi.org/10.1007/s11071-013-1127-x
32. Li Z, Yang Z, Peng Y, Zhu F, Ming X (2015) Prediction of chatter stability for milling process using Runge-Kutta-based complete discretization method. Int J Adv Manuf Technol 86(1-4):943–952. https://doi.org/10.1007/s00170-015-8207-7